Journal of the Meteorological Society of Japan, Vol. 76, No. 3, pp. 363–383, 1998

Possible Role of Symmetric Instability in the Onset and Abrupt Transition of the Asian Monsoon

By V. Krishnakumar[1] and K.-M. Lau

Laboratory for Atmospheres, NASA/Goddard Space Flight Center, Greenbelt, Maryland 20771, U.S.A.

(Manuscript received 7 July 1997, in revised form 25 March 1998)

Abstract

The physical connections between dry/moist (conditional) symmetric instability (SI/CSI) off equatorial diabatic thermal forcing, and the onset of the Asian monsoon are investigated using the Goddard Laboratory for Atmospheres general circulation model (GLA GCM). The objective of this study is two-fold: to elucidate the causal relationship between SI/CSI and monsoon onset, and to investigate the threshold behavior of asymmetric monsoonal thermal forcing under condition of SI/CSI. This work corroborates the authors' earlier linear instability analysis results, which show, that SI/CSI in the boreal summer monsoon basic states may be a plausible explanation for the abrupt monsoon transition.

Monsoon transitions in the model, as depicted by the abrupt meridional movement of the axis of maximum vertical motion from equator to northern latitudes, occur during 16–20 May for the East Asian Monsoon (EAM) and 1–5 June for the South Asian Monsoon (SAM) regions. The necessary stability criterion for dry (moist) SI over the EAM and SAM regions reveals a sudden cross equatorial advection of negative dry potential vorticity (DPV) and moist potential vorticity (MPV) into the summer hemisphere five to ten days preceding the model monsoon transition. This causes dry and moist SI. Maximum shift of the zero line of DPV and MPV (dry and moist symmetrically unstable regions) happens subsequent to monsoon transition. Simplified analysis of the potential vorticity (PV) budget equation reveals that the lower tropospheric negative PV advection into the summer hemisphere is largely governed by the dominance of vertical differential diabatic heating over horizontal differential diabatic heating.

The diabatic heating also shows an abrupt increase from 2–3 K day^{-1} before the transition, to 12–14 K day^{-1} at the time of monsoon transition. The genesis of pre-monsoon weak heat source arises primarily due to unstable SI and CSI of the pre-monsoon basic states, which consequently produce moderately large scale lower (upper) tropospheric convergence (divergence) patterns slightly poleward of the zero line of DPV and MPV. Lower tropospheric conditionally unstable tropical atmosphere, in the presence of off equatorial large scale lower (upper) tropospheric convergence (divergence), is conducive to exciting CISK-like processes, which may eventually release large amounts of latent heat and develop a strong heat source at the time of monsoon transition. We have noted that a fully established model meridional circulation originates only when the diabatic forcing magnitude exceeds some threshold value of around 5 K day^{-1} at the time of monsoon transition. The model transition is more pronounced over the EAM region than over the SAM region. The linear steady-state dynamical response of a zonally symmetric atmosphere as a consequence of varying the location and magnitude of an idealized asymmetric thermal forcing reveals that the most intense meridional circulation (maximum efficiency of vertical motion) is accomplished when the thermal forcing is located around 10°N. The interrelationship between the location of zero DPV/MPV contour, lower tropospheric maximum convergence versus maximum vertical velocity of the monsoonal circulation in the summer hemisphere, clearly suggests that SI (CSI) of zonal monsoon flows is a causal mechanism for the onset of monsoon transition.

1 Corresponding author: Dr. V. Krishnakumar, Space Applications Corporation, Code 913, NASA/Goddard Space Flight Center, Greenbelt, Maryland 20771, U.S.A.
©1998, Meteorological Society of Japan

1. Introduction

Theoretical, modeling, and observational studies in the past two decades have increased significantly the understanding of symmetric instabil-

ity (SI) and moist conditional SI (CSI). Investigations pertaining to SI and CSI received much attention because those using SI and CSI have had success in explaining diverse atmospheric phenomena. Theoretical bases of SI have been developed by Sawyer (1949), Kuo (1954), Eliassen (1952), Ooyama (1966), Stone (1966), Hoskins (1974), Emanuel (1979, 1983), Bennetts and Hoskins (1979), Dunkerton (1981, 1993), Stevens (1983), Sun (1984), Xu (1986) and many others. Dry SI in rotating fluids arises due to an imbalance of pressure gradient and Coriolis forces when the absolute value of angular momentum of a fluid parcel decreases with distance from the vertical axis (radius). CSI, which is often associated with slantwise convection, emerges from an imbalance of pressure gradient, Coriolis, and buoyancy forces in a baroclinic atmosphere. The necessary criterion for SI (CSI) is that the dry (moist) potential vorticity on an isentropic surface is negative in the Northern Hemisphere and positive in the Southern Hemisphere.

In most of the previous studies, researchers applied SI and CSI theories to explain a variety of extratropical atmospheric motions. There have been only a very few studies on the application of SI/CSI to tropical atmospheric motions. Using the low level MONEX (MONsoon EXperiment) data over the Indian Ocean region, Young (1981) showed that the possibility of inertial instability existed between the zero-line of absolute vorticity (around 10°N) and the equator. Krishnakumar and Keshavamurty (1993) investigated the possibility of SI of mean July monsoon zonal flows, including a simple parameterized cumulus heating, and found unstable modes with doubling time and periods of oscillation around 1–2 days. Lau and Li (1984) and Lau *et al.* (1988) found that the movement of the East Asian monsoon rainfall band appeared to jump between stationary positions from lower latitudes to higher latitudes on short time scales during the boreal spring (mid-May). More recently, using GMS infrared data for 1982 to 1987, Hirasawa *et al.* (1995) found that abrupt seasonal change in the characteristics of the cloud zone over East Asia occurred around the middle of May.

To investigate the physical mechanisms governing the features of the abrupt transition of the monsoon meridional cell, Krishnakumar and Lau (1997) (hereafter KL) performed stability analysis with a zonally symmetric multi-level moist linear model using the climatological monthly European Centre for Medium Range Weather Forecasts (ECMWF) basic flows of January to December as well as ECMWF pentad mean zonal flows starting from 1–5 May to 26–30 June. In the absence of cumulus heating, KL found that the linear stability of the monsoon flow changed dramatically with the emergence of many unstable modes in the month of May, and with the inclusion of cumulus heating, unstable modes appeared in summer monsoon months (May–August) with substantially enhanced growth rates. One of the key findings of KL's analyses is that the unstable modes resulting from SI emerged at about the right time (May) and cumulus heating significantly enhanced the growth rate. The abrupt nature of the monsoon transitions was also clearly seen in the ECMWF pentad mean meridional circulation in the South Asian monsoon region. Lau and Yang (1996) (henceforth LY96) studied the onset, abrupt transitions, and development of the summer monsoon system using data from a 10-year integration with the Goddard Laboratory for Atmospheres atmospheric (GLA) General Circulation Model (GCM). Linear SI calculations from KL's model of the mean basic zonal flows (averaged from the 10-year climatology of the GLA GCM) in the longitude sector for East Asia (110°E–120°E) revealed that inherent instability was present in the basic monsoon flow in May before the monsoon circulation was fully developed (see LY96). However, KL's model did not explicitly clarify the issue of causality between SI and monsoon onset. Thus, modeling and theoretical studies support the notion that rapid monsoon transition may be attributed to SI of the late boreal-spring mean basic flows.

There have also been recent studies regarding the location and origin of a near-equatorial convection zone like the ITCZ. Waliser and Somerville (1994) studied the preferred latitude zone of the ITCZ using a thermally forced shallow-water model and argued that the low-level momentum balance conditions between meridional pressure gradient, Coriolis force, and frictional forces, can explain the off equatorial convergence maximum and ITCZ. Tomas and Webster (1997) examined the role of inertial instability in determining the location and strength of near-equatorial convection. They noted that in regions where there was a weak cross-equatorial surface pressure gradient, the convection was close to the equator and generally located over the warmest sea-surface temperature (SST), where the zero line of the absolute vorticity also lied closer to the equator. In regions where there was a strong cross-equatorial pressure gradient (such as the South Asian monsoon region), the convection (ITCZ cloud zone) was off the equator and not directly above the warmest SST. Here, the zero line of the absolute vorticity also resided off the equator up to 10° into the summer hemisphere (inertially unstable region). There have been a number of important studies on the understanding of the dynamics of symmetric circulation driven by tropical heating (*e.g.*, Charney, 1973; Schneider and Lindzen, 1977; Held and Hou, 1980; Lindzen and Hou, 1988; Hou and Lindzen, 1992; Plumb and Hou, 1992; Satoh, 1994).

Another interesting possibility for the abrupt na-

ture of the onset of meridional circulations with regard to its sensitivity to prescribed thermal forcing has been discussed by Plumb and Hou (1992) (hereafter PH92). PH92 noted that, in response to an asymmetric heat source, there was a transition from a state of thermal equilibrium with no meridional flow to a state where strong meridional circulation existed. A nonlinear angular momentum conserving circulation existed only when the off-equatorial forcing exceeded a certain threshold. The applicability of PH92's model to explaining realistic phenomena such as monsoon onset is questionable due to a major model limitation: the thermal forcing was externally prescribed and hence noninteractive. It is apparent that such a model cannot explain the origin and location of the off equatorial heat source. This limitation could, in principle, be eliminated if one employed a sophisticated GCM. PH92 also did not address the issue of SI and it is conceivable that their model behavior may change due to the important dynamical effects arising from SI in the nearby equatorial regions. In the inviscid limit of Held and Hou's (1980) axisymmetric model, the condition for SI of the circulation was satisfied.

One of our main aims with this study is to address why a connection should exist between SI and monsoon onset. Linear instability analyses of KL showed that the linear stability of the flow changes rapidly at the monsoon onset time, which suggested that SI of zonal monsoon flows may be a possible candidate for the sudden monsoon transition. However, KL's linear instability analyses had the limitation that it could not explicitly address the physical connection between SI and the monsoon onset, especially the important question of causality between SI and monsoon onset. In this study, we also investigate the possible connection between monsoon onset and critical thermal forcing using a complete GCM, in the overall perspective of SI.

In the present study, using the GLA GCM, the possible role of SI in monsoon transition is investigated. We have addressed primarily two major issues: (i) the causal relationship between SI/CSI and monsoon onset and (ii) the threshold behavior of the asymmetric monsoonal thermal forcing under condition of SI/CSI. We have performed two integrations for the summer monsoon months (May–September) for two years, 1987 and 1988. In order to compare the linear response of a zonally symmetric atmosphere to monsoonal diabatic heating, a simple multi-level zonally symmetric model has been used. In Section 2, we describe briefly the GLA GCM details and the numerical simulations performed. The main results are presented in Section 3. A separate discussion on the simulated monsoon transitions is given in Subsection 3.1. The role of SI is elucidated in Subsection 3.2 and the response of monsoon circulation to asymmetric diabatic forcing is explained in Subection 3.3, where both the nonlinear and linear results are presented. Further discussion and conclusions are provided in Section 4.

2. Model details and numerical simulations

The model used for this investigation is the latest version of GLA GCM with the inclusion of gravity wave drag (GWD) parameterization (see Zhou *et al.*, 1996). The discussion here is brief since the model has been extensively documented in other papers. GLA GCM has a horizontal resolution of 4° latitude ×5° longitude and 17 sigma layers in the vertical. The model uses a modified version of the Arakawa-Schubert cumulus parameterization discussed in Sud *et al.* (1991) with an explicit parameterization for rain evaporation and cumulus downdrafts by Sud and Walker (1993). The land surface processes are parameterized using a simple biosphere (SiB) model. All the other detailed parameterization schemes used in this model are enumerated in Sud and Walker (1993) and Kim and Sud (1993). Recently, LY96 and Yang *et al.* (1996) analyzed GLA GCM data for the Atmospheric Model Intercomparison Project (AMIP) period (1979–1988) and found that the model provided reasonably realistic simulations on the intraseasonal and interannual variability associated with the Asian summer monsoon. Zhou *et al.* (1996) studied the influence of orographically induced GWD in the GLA GCM and found several positive impacts on the simulation of monsoon circulation and precipitation patterns.

We have carried out two integrations (May to September) for the years 1987 and 1988. In the two simulations, we used ECMWF analyses as initial conditions corresponding to 00Z 01 May 1987 and 1988, respectively, and in both cases the model was integrated till the end of September. Since our primary objective is to study the physical mechanism of monsoon transition in the model, we have focused only on the transition months May and June. Figures 1a–1d show latitude-time cross sections of the simulated pentad rainfall starting from May 1 to June 30 for two longitudinal bands (i) 70°E–90°E, which is representative of Indian subcontinent, and (ii) 90°E–110°E, which is representative of Indo-China and SE Asian regions for 1987 and 1988. The simulated Indian monsoon rainfall for 1987 (Fig. 1a) and 1988 (Fig. 1b) is characterized by a sudden increase in rainfall at the time of model monsoon onset, which happens around the first week of June (pentad 7). Around the onset period for 1987, the model predicts excess rainfall around 5°S and the ITCZ rainfall pattern exhibits a bimodal structure. The transition of the ITCZ from the equator to 10°–15°N is rather abrupt in 1987 (Fig. 1a), gradual in 1988. Significant differences in the overall rainfall amount are particularly noticeable over the entire monsoon regions during 1987 and 1988. The oc-

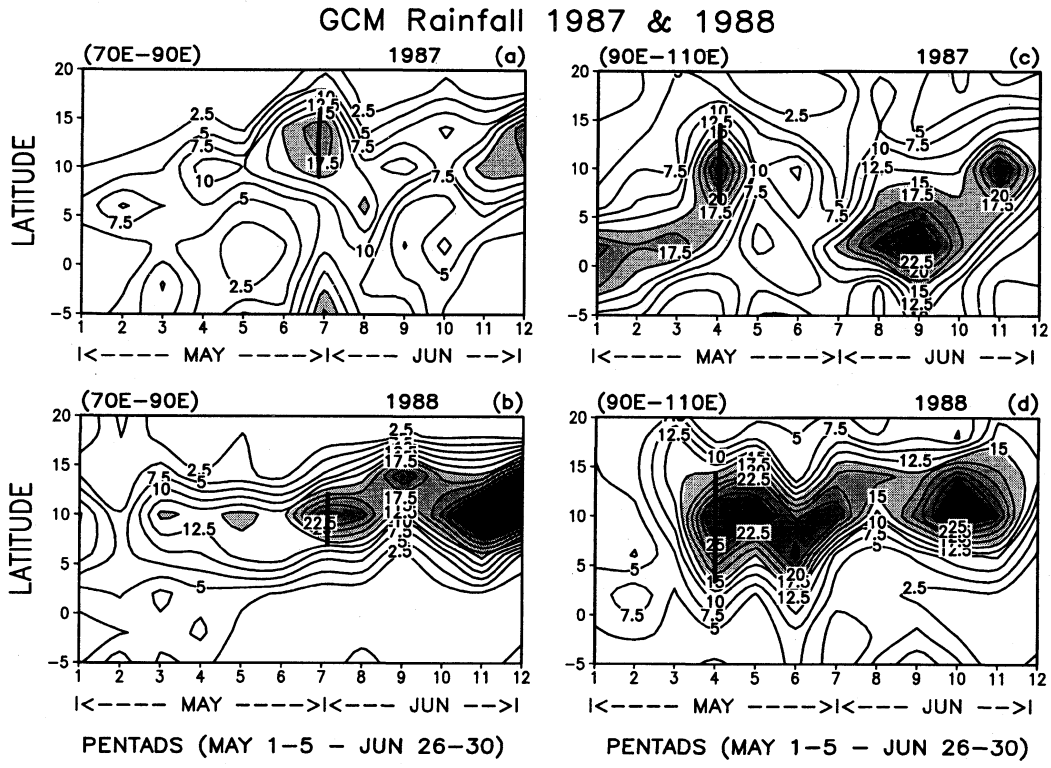

Fig. 1. Time-latitude cross section of sumulated 5-day mean rainfall (mm day^{-1}) from May 1 to June 30 for (i) Indian subcontinent (70°E–90°E) for (a) 1987 and (b) 1988 (ii) Indo-China and SE Asian regions (90°E–110°E) for (c) 1987 and (d) 1988. Values larger than 15 mm day^{-1} are shaded. The occurrence of the model monsoon onset is denoted by thick solid line.

currence of the model monsoon onset is denoted by the thick solid line in Figs. 1a–1d. Based on real data, the year 1987 was observed to be a deficient monsoon (less than normal rainfall) while the year 1988 was an excess monsoon (heavier than normal rainfall). Comprehensive analyses describing the important differences in the development of the monsoon system during these two contrasting years were carried out by several researchers previously (*e.g.*, Krishnamurti *et al.*, 1989, 1990; Palmer *et al.*, 1992; Fennessy *et al.*, 1994). The GLA GCM simulates reasonably well the deficient as well as excess monsoonal rainfall distribution that was observed. The large scale global features are reasonably well simulated by the GLA GCM when compared to the available observed data sources (see LY96 for GLA GCM intraseasonal and synoptic-scale climatology). Another noteworthy characteristic is the presence of 15–20 days oscillation in the ITCZ rainfall from around 10°N to 15°N.

The rainfall distribution in the Indo-China and Southeast Asian regions for 1987 (Fig. 1c) shows a gradual northward shift of the ITCZ from the equator to 10°N with a sharp increase in rainfall at the time of monsoon onset which happens around mid of May (pentad 4). The characteristic feature of the onset phenomenon for 1988 (Fig. 1d) is an abrupt increase in rainfall around the middle of May (pentads 4 and 5), unlike the sluggish monsoon onset of 1987 (Fig. 1c). The simulated monsoon rainfall during the years 1987 and 1988 over Indo-China and SE Asia revealed that during 1987, much less rainfall occurred, and during 1988 much heavier rainfall occurred over most of the regions, essentially bringing out the contrasting nature of the two years. The SE Asian monsoon also exhibits a 15–20 day oscillation similar to the Indian band. We have also examined many dynamical fields produced by the GLA GCM to study the evolution and other characterestics of these two contrasting summer monsoons of 1987 and 1988. We have found that the model reproduces reasonably well both the spatial and temporal variability of the Asian summer monsoon. These results have shown that abrupt monsoon transitions occur, albeit with different details in both strong and weak monsoons.

3. Model results

This and the following sections are devoted to the understanding of the physical mechanisms of monsoon transition produced in the GLA GCM for the active monsoon year of 1988, during which the onset (transition) is very abrupt. Our later references to the time period will include only 1988. The results

are presented mainly for the two longitudinal bands (i) 90°E–120°E and (ii) 70°E–100°E. The former is representative of East Asian monsoon regions (hereafter EAM) and the latter South Asian and Indo-China regions (hereafter SAM). We have mainly focused on the physical connection between SI as well as moist SI and monsoon onset and its causal relationship. We also present some results demonstrating the plausible connection between monsoon transition and off-equatorial, critical thermal forcing as discussed in Section 1.

3.1 Monsoon transitions

Monsoon transition refers to the sudden meridional movement of the axis of the maximum vertical motion and the associated cloud and rain bands from one latitudinal position to another. It may be used to describe the monsoon onset, in which the rainband jumps from the equatorial ITCZ to about 10°–15°N. For the EAM, a second jump of the rainband from 10°–15°N to 25°–30°N is often observed (Lau and Li, 1984; Lau *et al.*, 1988). But this second jump is not well simulated in the GLA GCM. In the following analysis, we focus only on the early onset stage *i.e.*, May–June period. Extensive documentation of the synoptic features associated with the onset of southwest monsoon over southern India is given in Ananthakrishnan *et al.* (1968). Some of the salient characteristic features of the onset phenomenon are an increase in rainfall, a strengthening of the low-level southwesterlies, an abrupt increase in moisture and the subsequent deepening of the moist layer.

Figure 2 shows the development of 5-day mean latitude-pressure ($y - p$) cross section of the zonal wind and meridional circulation in the EAM region beginning 1–5 May and ending 26–30 May, 1988. The shadings (right panels) indicate the regions of maximum vertical motions (ω) and only values larger than -5×10^{-2} Pa s^{-1} are darkened. One of the important features to be noted in Fig. 2 is the abrupt shift of the axis of the maximum vertical motions from the equatorial latitudes ($\approx$ 2°N) before the transition period (6–10 May) to the northern latitudes ($\approx$ 10–15°N) at the time of transition (16–20 May). The evolution of pentadal mean vertical velocity distribution in the EAM region is examined separately in Subsubsection 3.2.3. It displays distinctly the sudden strengthening at the time of monsoon transition (see also Fig. 6, right panel). The model onset of EAM takes place during 16–20 May as depicted by the presence of marked meridional circulation with strong ascending motion around 10°N. During the EAM onset period, the low-level westerlies from the equator to 15°N strengthen rapidly together with an enhancement of the upper tropospheric easterlies (Fig. 2d, left panel). Baroclinic and barotropic shears begin to develop from 11–15 May and continue for the remaining period (Fig. 2c, left panel). The vertical and horizontal shears become very pronounced at the time of onset 16–20 May and continue with same or enhanced intensities for the later periods. It is also interesting to see the northward migration and weakening of the subtropical upper tropospheric westerlies from 25°N during the onset period (16–20 May) to high latitudes (> 35°N, not shown) during the post onset period (26–30 May). By 26–30 May, the vertical motions are extended poleward to about 25°N. Lau and Li (1984) and Lau *et al.* (1988) observed such abrupt transitions in zonal wind and rainfall over central and eastern parts of China marking the arrival of *Mei-Yu* onset. A detailed review of the East Asian summer monsoon characteristics and its impact on global climate teleconnection is given by Lau (1992). Similarly for the SAM region, the evolution of the zonal wind and meridional cell from the beginning of May to mid June indicate that the low level westerlies and vertical motions begin to strengthen from 11–15 May around 5°N to 10°N and maintain their amplitude until 26–30 May (not shown). A rapid northward progression of the vertical motions from 5°N–10°N to 15°N with an enhanced westerly jet of around 15 m^{-1} takes place during 1–5 June, illustrating the onset of SAM. Similar transition features with less amplitude are found for the 1987 model simulation (not shown).

3.2 Role of symmetric instability

We now consider the role of SI and CSI in monsoon transition over EAM and SAM regions. Here, we argue that an apparent connection exists between SI and the monsoon onset. One of the important issues to be addressed is whether SI (CSI) commences preceding the actual monsoon transition (onset) and this is particularly important to understand the causal relationship between SI and monsoon onset.

3.2.1 Stability criterion

This section provides a rudimentary treatment of SI. Readers who are familiar with the SI concept may proceed directly to Subsubsection 3.2.2.

From a Lagrangian perspective *i.e.*, by considering forces acting on individual fluid parcel, an expression can be derived measuring the stability of a parcel with respect to horizontal displacements with the geostrophic basic wind (U_g), using the assumption that geostrophic parcel displacement does not perturb the pressure field (see Holton, 1992 for all the details). The condition for inertial instability of such a parcel is given by

$$f\frac{\partial M}{\partial y} < 0 \quad \text{or} \quad f\eta < 0 \tag{1}$$

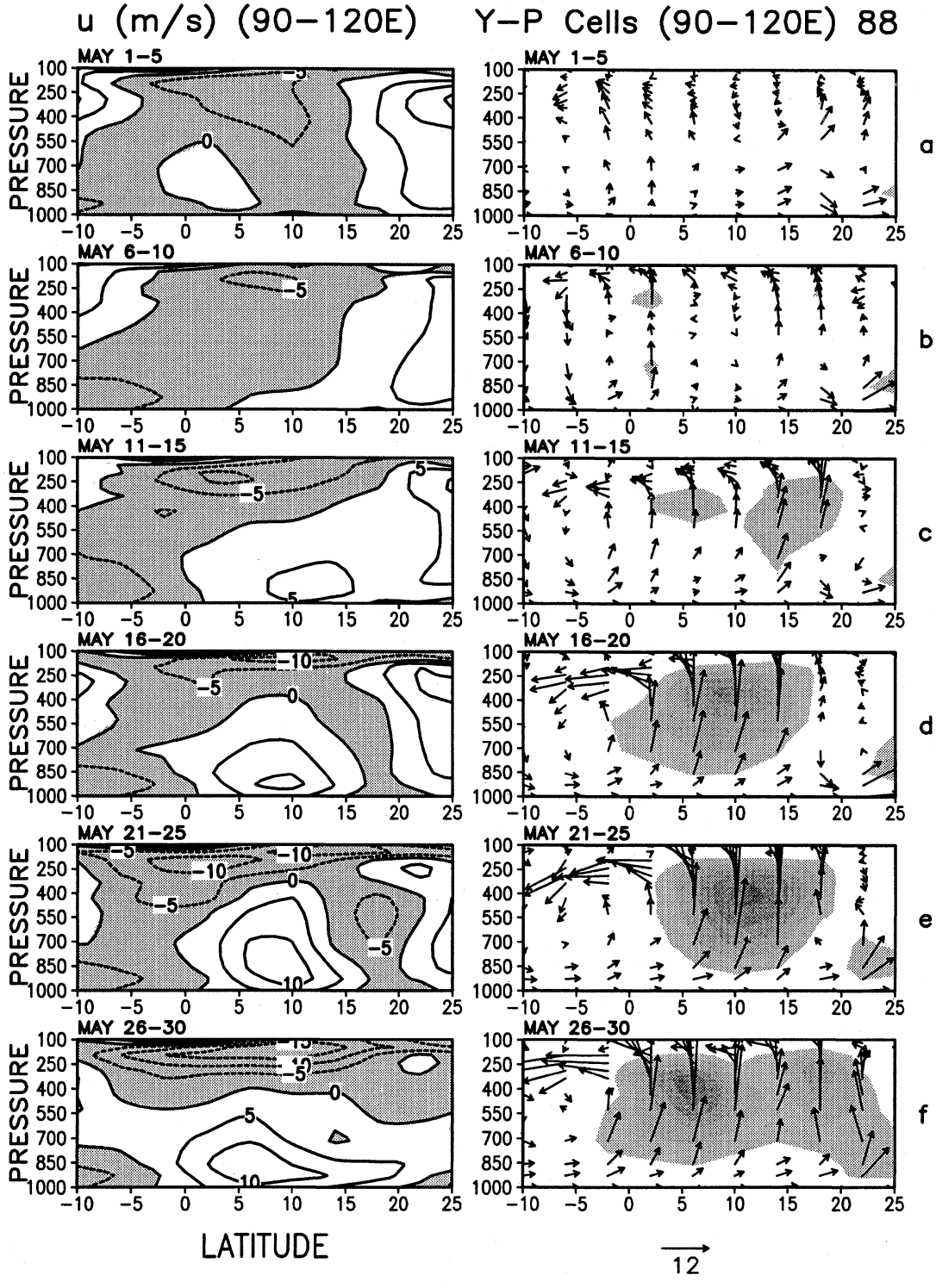

Fig. 2. Latitude-pressure cross sections of pentad mean zonal wind (left panels) and meridional circulation (right panels) over the East Asian monsoon region (EAM; 90°E–120°E) for 1988. The vertical motion has been amplified by 100 times in the plots. The shadings (right panels) denote regions of negative vertical velocity with values $\geq -5 \times 10^{-2}$ Pa s^{-1}. Contour interval for the zonal wind is 5 m s^{-1} and negative values are shaded.

where $M \equiv fy - U_g$ is the absolute zonal momentum and $\eta = \zeta + f = -\frac{\partial U_g}{\partial y} + f$. Here η is the absolute vorticity, ζ is the relative vorticity and f is the Coriolis parameter. In the region of inertial instability in the northern hemisphere (since f is positive), ζ is negative. The instability in this case will redistribute absolute zonal momentum so as to reach a dynamically stable configuration in which

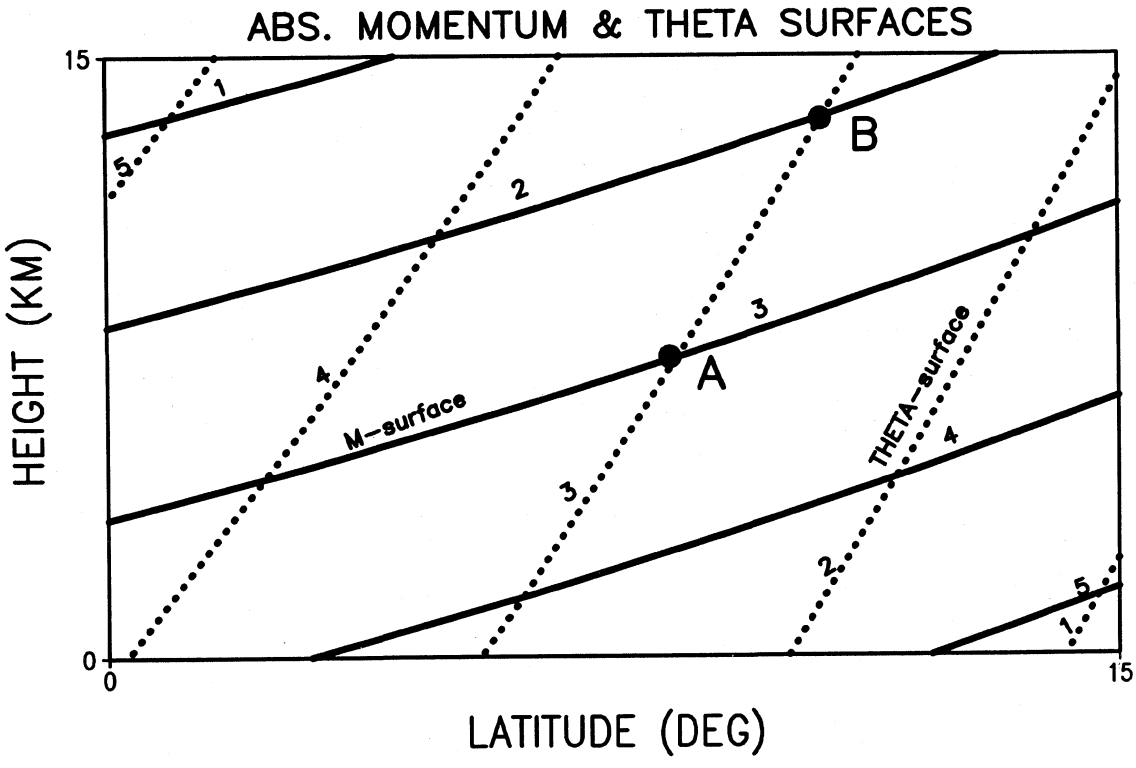

Fig. 3. Schematic latitude-height cross section showing isolines of absolute momentum (M; heavy bold lines) and potential temperature (Θ; dotted lines) for a dry symmetrically unstable basic state. See Subsubsection 3.2.1 for details.

M increases with distance from the vertical axis of rotation.

If parcels are displaced along slantwise paths rather than vertical or horizontal paths and if it is assumed that the mean wind is directed along the x-axis and is in thermal wind balance condition, it can be shown that the stability of such motions depends on the relative slope of the potential temperature (Θ) and M surfaces (Holton, 1992). Solberg (1936) referred dry SI to a type of dynamic instability as inertial instability along an isentropic surface. Dry SI arises only in the presence of vertical shear of the mean horizontal wind in which the perturbations are independent of the coordinate parallel to the mean flow. The equivalent instability criterion as compared to (1) now becomes

$$f\left(\frac{\partial M}{\partial y}\right)_{\Theta} < 0 \tag{2}$$

where the parcel displacements are along Θ surfaces. In terms of Ertel potential voriticity, Charney (1973) showed that a basic state of the type $U = U(y,z)$ on a β-plane is unstable to zonally symmetric disturbances if

$$f\,P < 0 \tag{3}$$

somewhere, where

$$P = \frac{1}{\rho_o}\left\{\frac{\partial U}{\partial z}\frac{\partial \Theta}{\partial y} + \left[-\frac{\partial U}{\partial y} + f\right]\frac{\partial \Theta}{\partial z}\right\} \tag{4}$$

is the Ertel potential vorticity of the basic state. Here ρ_o is the mean density, Θ is the basic state potential temperature, $\frac{\partial U}{\partial y}$ is the horizontal wind shear and $\frac{\partial U}{\partial z}$ is the vertical wind shear. Equivalent to the stability criterion (3) is the Richardson number

$$Ri < \frac{f}{\left(f - \frac{\partial U}{\partial y}\right)} \tag{5}$$

The condition (5) is obtained from (3) by making use of the thermal wind relationship $\frac{\Theta}{g}\frac{\partial U}{\partial z} = -\frac{1}{f}\frac{\partial \Theta}{\partial y}$. Here $Ri \equiv \frac{N^2}{(\partial U/\partial z)^2}$ where N is the buoyancy ($Brunt - Väisällä$) frequency, *i.e.*, $N^2 = g\frac{\partial \ln \Theta}{\partial z}$. It can be shown that an atmosphere with the condition (5) or (3) in geostrophic balance must have Θ surfaces steeper than the M surfaces (Holton, 1992). Figure 3 shows a schematic (y,z) cross section displaying isolines of M and Θ for a dry symmetrically unstable basic state. Solid lines (dotted lines) are absolute momentum (potential temperature) surfaces where the values increase (decrease) from upper levels to lower levels. Note that the Θ surfaces slope more than the M surfaces as a requirement of slantwise instability. For a slantwise displacement of a parcel along an isentropic surface shown schematically by points A and B, the motion is said to be unstable since M decreases with latitude along the path as per the criterion for dry SI

(2).

The necessary condition for dry SI in a balanced atmosphere is that the dry potential vorticity (DPV) of the basic flow (here, the 5-day summer monsoon mean flows starting from 1–5 May to 26–30 June) on an isentropic surface is negative (positive) in the Northern (Southern) Hemisphere. DPV of the basic flow is given by

$$P = -g\left\{\underbrace{\frac{\partial U}{\partial p}\left(\frac{\partial \Theta}{\partial y}\right)_p}_{P_V} + \underbrace{\left[-\left(\frac{\partial U}{\partial y}\right)_p + f\right]\frac{\partial \Theta}{\partial p}}_{P_H}\right\} \tag{6}$$

where U and Θ are the pentad mean zonal wind and potential temperature, respectively, averaged over the EAM and SAM regions. The two parts of (6), reading from left to right, are the contributions of DPV due to both vertical (P_V) and horizontal (P_H) shear of the mean zonal wind. The subscript p in (6) denotes that derivatives are taken on constant pressure surfaces. Here, we have assumed that the variation of potential temperature on an isobaric surface is small. Recent analysis by Tomas and Webster (1997) have shown that in the near equatorial region, potential temperature variation on an isobaric surface is small, which implies approximate correspondence between isentropic and isobaric surfaces.

Observations show that tropical (monsoonal) lower tropospheric atmosphere is largely, conditionally (*i.e.*, the instability is conditional to saturation of the air parcel) unstable. At the time of monsoon onset, a dramatic increase in moisture and subsequent deepening of the moist layer are imminent and, therefore, moist SI conditions are more dominant than DSI. For a parcel to be unstable, the equivalent potential temperature (Θ_e) surfaces must be steeper than the M surfaces by arguments analogous to DSI, as was described in detail before. The necessary condition for CSI, *i.e.*, the moist potential vorticity (MPV) of the basic flow (here, the 5-day summer monsoon mean flows starting from 1–5 May to 26–30 June) on an isentropic surface is negative (positive) in the Northern (Southern) Hemisphere. MPV (P_m) of the basic flow is same as (6) but with Θ replaced by Θ_e the equivalent potential temperature. Θ_e has been derived from specific humidity and temperature fields. When an air parcel reaches saturation point in a region of negative MPV but is devoid of conditional or potential instability (CI), slantwise overturning occurs due to CSI. Therefore, it is important to delineate the effects of CI from CSI.

3.2.2 Stability conditions for the Asian monsoon

Calculations were carried out for both the EAM and SAM. The circulation of the two regions are basically similar in their dynamical properties. For brevity, only results for EAM will be highlighted. Figure 4 (left panel) shows the latitude-pressure cross sections of the evolution of DPV (calculated from (6) for the EAM region). The striking feature here is the sudden cross equatorial advection of negative DPV (note the shaded regions in the summer hemisphere (SH)) from the Southern Hemisphere to the Northern Hemisphere during 11–15 May, just preceding the model monsoon transition (16–20 May), thereby satisfying the condition for dry SI. Before the monsoon transition (1–5 May and 6–10 May), the zero line of DPV (denoted by thick contour) resides very close to the equator showing only very small regions of dry SI in the proximity of the equator. Beginning 11–15 May, the zero line of DPV shifts up to 5°N into the SH with a vertical extension from 1000 hPa to 400 hPa, thereby setting the condition for dry SI. During the model monsoon onset period (16–20 May), the symmetrically unstable region extends both latitudinally (6°–7°) and vertically (1000 hPa to 250 hPa). Maximum shift of the zero line of DPV occurs subsequent to monsoon transition (21–25 May). Large areas of negative DPV covering the entire troposphere from equator to 8°N with a maximum DPV value of around -2.5×10^{-7} m^{2}s^{-1}K kg^{-1} are found. The next pentad (26–30 May) shows a slightly equatorward displacement of the zero line of DPV from its earlier position. Dry SI conditions (note the shaded regions in the Southern Hemisphere) are also satisfied in the upper tropospheric regions ($\approx$ 400 hPa to 100 hPa) of the winter hemisphere (WH) from the equator to 15°S. This is supposed to generate mid-tropospheric convergence and updrafts in the WH over symmetrically unstable regions. Only weak vertical motions exist over such regions in the WH, as shown in Figs. 2 and 6 (right panels), presumably because of high static stability values prevailing in the upper troposphere inhibiting strong vertical motions.

Figure 4 (right panel) shows the latitude-pressure cross sections of the evolution of MPV fields (calculated from P_m) denoted by thin solid (positive values) and dashed (negative values) lines and the zero contour in thick solid line. Also displayed are the contours of $\partial\Theta_e/\partial p$ as denoted by thick dotted lines. $\partial\Theta_e/\partial p > 0$ represents conditionally unstable regions, and $\partial\Theta_e/\partial p < 0$ represents conditionally stable regions. It is apparent from Fig. 4 that the criterion for CI (see the positive contour 0.5) is satisfied for all the pentads starting from 1–5 May through 26–30 May over the entire tropical lower troposphere ($\approx$ 1000 hPa–750 hPa) extending latitudinally from 5°S–15°N. Negative MPV (thin dashed contours) over conditionally unstable regions exists in the SH from 1–5 May to 26–30 May. According to CSI theory, a saturated air parcel in a region with negative MPV but in the absence of CI

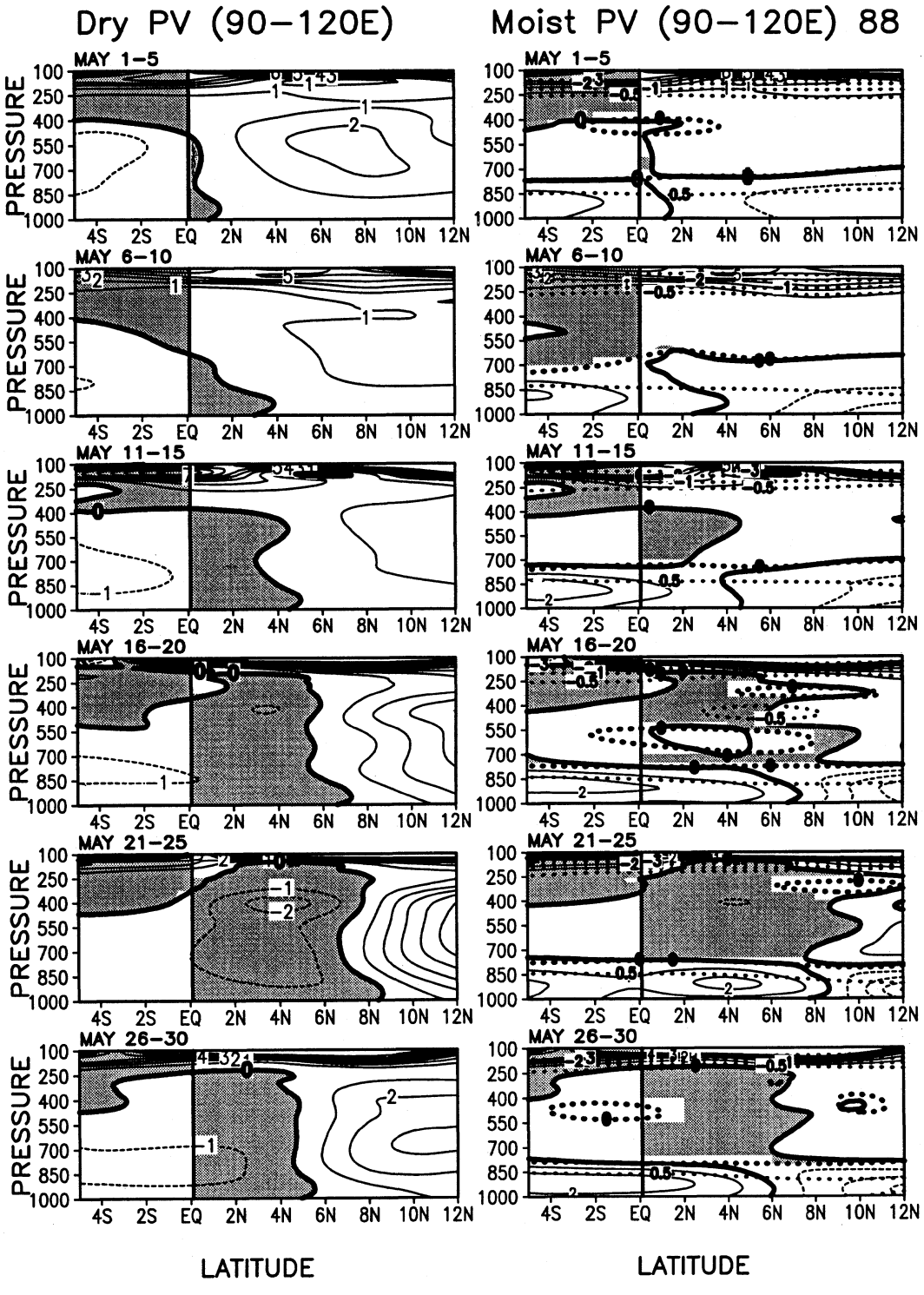

Fig. 4. Latitude-pressure cross sections of (i) dry potential vorticity (DPV) (left panels) calculated using the GLA GCM pentad mean profiles of zonal wind and potential temperature (ii) moist potential vorticity (MPV) (right panels) calculated using the pentad mean model profiles of zonal wind and equivalent potential temperature over the EAM region for 1988 at intervals of 10^{-7} K $m^2kg^{-1}s^{-1}$. On the left (right) panels, thin solid and dashed lines denote positive and negative DPV (MPV) contours respectively. The heavy bold line represents the zero DPV (MPV) contour and the shaded areas denote dry (moist or conditional) symmetrically unstable regions. On the right panels, the thick dotted line represents contours of $\partial\Theta_e/\partial p$ at intervals of 10^{-3} K Pa^{-1}.

will be subject to CSI leading and to slantwise overturning. These unstable CSI regions are shaded in Fig. 4 (right panel). It should be noted that negative MPV regions in the absence of CI (unstable CSI regions) are practically missing well before the monsoon transition in the SH (see pentads 1–5 May and 6–10 May). One of the distinctive features to be noted is the sudden advection of negative MPV (as revealed by the shift of the zero MPV contour) into the SH between the region ($\approx$ 700 hPa–400 hPa; equator-4°N) by 11–15 May (just preceding to monsoon transition), thereby initiating unstable CSI regions. At the time of monsoon transition (16–20 May), the zero line of MPV extends both latitudinally and vertically into the SH (see the shaded regions between $\approx$ 700 hPa–250 hPa; equator-9°N). Note also a small region ($\approx$ 750 hPa–550 hPa; 2°S–9°N) where CI is present (zero contour in thick dotted line). By 21–25 May, as depicted by the shift of zero MPV contour encompassing the area between equator to $\approx$ 10°N and 700 hPa–150 hPa, broad regions of negative MPV have developed. By 26–30 May, the zero MPV contour in the SH begins to shift slowly equatorward. Note that there exists large unstable CSI regions (shaded areas) in the upper tropospheric WH as in the case of DPV distribution. The upper tropospheric MPV pattern over the WH is remarkably closer to the corresponding DPV pattern, which is not surprising because Θ and Θ_e have very little change in the upper tropospheric regions due to diminishing moisture content. For the SAM region, the DPV and MPV variations are similar to EAM except that the DPV/MPV advection starts three/four pentads (11–15 May) prior to SAM transition (1–5 June) (not shown). The zero contour of DPV (MPV) resides in and around 9°N in the SH and remains a quasi-permanent feature till the end of June (not shown). KL's stability analysis using the ECMWF monthly climatological profiles also showed a similar feature for the July mean conditions over the SAM regions.

It is evident from Fig. 4 that unstable SI and CSI conditions are established preceding the monsoon transition and remain as a quasi-permanent feature for a long time after the monsoon transition. We now briefly discuss the dominant processes that govern the shift of the zero DPV and MPV contours into the SH. This can be illustrated by performing a diagnostic analysis of the PV budget equation. In our simplified PV budget analysis, we focus only on the contribution due to diabatic heating terms; the frictional dissipation terms are not considered. It should be mentioned here that in order to obtain a comprehensive scenario of the negative DPV and MPV generation before and after the monsoon transition, a detailed diagnostic study of the time evolution of DPV and MPV equations elucidating the relative importance of all terms is required. Neglecting frictional effects, the Lagrangian rate of change of DPV is given by

$$\frac{dP}{dt} = -g\left\{\underbrace{\frac{\partial U}{\partial p}\left(\frac{\partial \dot{Q}}{\partial y}\right)_p}_{\text{TermA}} + \underbrace{\left[-\left(\frac{\partial U}{\partial y}\right)_p + f\right]\frac{\partial \dot{Q}}{\partial p}}_{\text{TermB}}\right\} \tag{7}$$

where $\frac{d}{dt} = \frac{\partial}{\partial t} + v\frac{\partial}{\partial y} + \omega\frac{\partial}{\partial p}$ and $\dot{Q} = \partial\Theta/\partial t$ represents the total diabatic heating. A detailed discussion of the pentadal mean evolution of $\dot{Q}$ distribution over the EAM and SAM regions is provided in Subsubsection 3.2.3. The two parts of (7), reading from left to right, represent the generation of DPV by horizontal (Term A) and vertical (Term B) differential diabatic heating. Note that Term A (Term B) contains the vertical (horizontal) shear of the mean zonal wind. For simplicity, we examine here the relative contributions of (7) at one pressure level (950 hPa) for a particular pentad corresponding to 16–20 May. We have seen from the DPV distribution (*cf.* Fig. 4, left panel) that the zero line of DPV shifts up to 7°N into the SH on 16–20 May. Figure 5a shows the contributions to DPV due to horizontal (P_H) and vertical (P_V) shear calculated from (6) at 950 hPa for the EAM at the time of transition (16–20 May), plotted as a function of latitude. Also shown in Fig. 5a is the total DPV labelled $P(P = P_H + P_V)$. The contribution due to P_H is about one to two orders of magnitude larger than that due to P_V, and this is generally true at all levels. The contribution from P_V can become significant in conjunction with strong baroclinic shear and weak barotropic shear. The curves for the total, P and P_H show similar characteristics with negative values from equator to about 7°N. The DPV budget (Fig. 5b) from (7) indicates that Term B (Term A) negatively (positively) contributes from equator to about 7°N (2°N to about 9°N). The decrease in total DPV at 950 hPa from equator to about 5–6°N and the increase in total DPV from 7°N and beyond (*cf.* Fig. 5a) are caused by the dominance of vertical differential diabatic heating (Term B) over horizontal differential diabatic heating (Term A) as shown in Fig. 5b. Note also that the local rate of change of P is given by the sum of the meridional advection term ($-v\frac{\partial P}{\partial y}$) and the vertical advection term ($-\omega\frac{\partial P}{\partial p}$). The effect of the meridional advection term at 950 hPa from the equator to 12°N is to decrease the local DPV (areal mean value -4.6×10^{-13} m^{2}s^{-2}K kg^{-1}). The vertical advection term contributes positively (negatively) from the equator to 7°N (7°N to 12°N) with an areal mean value 0.5×10^{-13} m^{2}s^{-2}K kg^{-1} (-0.9×10^{-13} m^{2}s^{-2}K kg^{-1}). Since Term B includes the horizontal shear of the mean zonal wind,

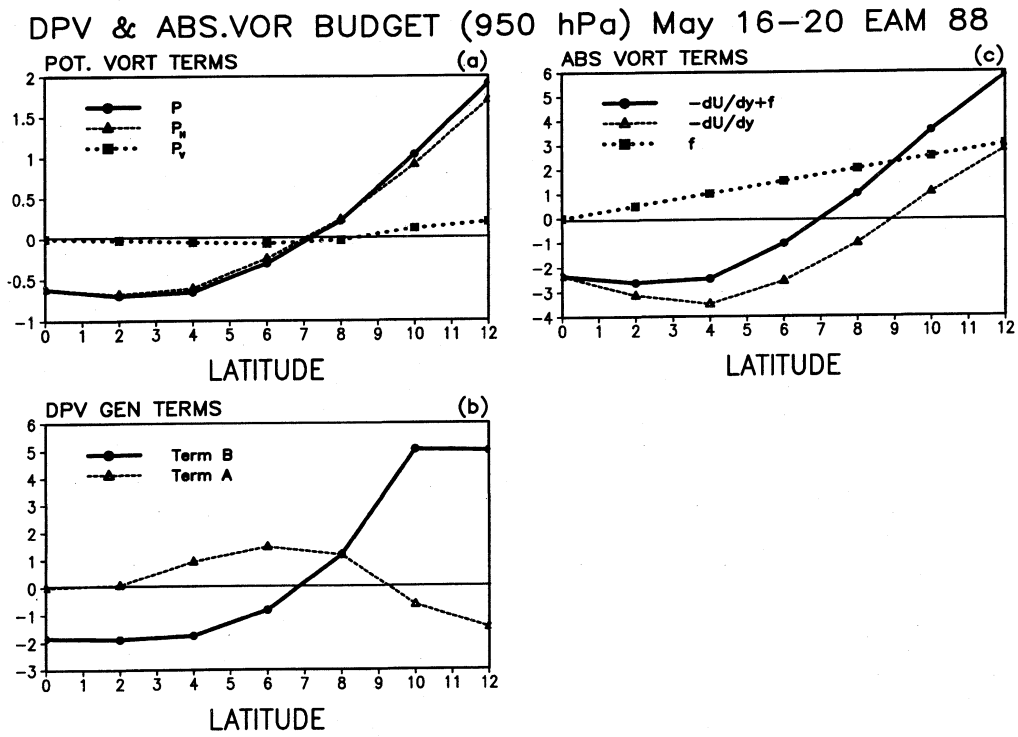

Fig. 5. Values at level 950 hPa for the EAM of (a) total DPV P (thick solid line with closed circles, 10^{-7} K m^2 kg^{-1}s^{-1}), contributions to P due to horizontal shear P_H (thick dashed line with open triangles) and vertical shear P_V (thick dotted line with closed squares) (b) DPV generation by horizontal (Term A, thick dashed line with open triangles, 10^{-13} K m^2 kg^{-1}s^{-2}) and vertical (Term B, thick solid line with closed circles) differential diabatic heating from equation (7) and (c) absolute vorticity (η, thick solid line with closed circles, 10^{-5} s^{-1}), contributions to η due to horizontal shear ($-\partial U/\partial y$, thick dashed line with open triangles) and Coriolis parameter (f, thick dotted line with closed squares) plotted as a function of latitude from equator to 12°N.

it is instructive here to discuss the variation of absolute vorticity ($\eta = (-\partial U/\partial y)_p + f$) at 950 hPa for the same pentad (16–20 May). Figure 5c shows the variation of f, horizontal shear $(-\partial U/\partial y)_p$ and η terms as a function of latitude. Three main features can be immediately noted from Fig. 5c: (i) negative values for η from equator to 7°N (location of the zero DPV contour at 950 hPa) (ii), negative values for $(-\partial U/\partial y)_p$ (anticyclonic shear) from equator to 9°N (location of the westerly jet at 950 hPa; *cf.* Fig. 2, left panel), and (iii) f is positive in the Northern Hemisphere. It is important to note that inertial destabilization (stabilization), or unstable (stable) SI regions, occur in the lower troposphere in regions of increasing anticyclonic (cyclonic) shears. The evidence of this feature was shown by Persson and Warner (1995) in an idealized, unforced CSI modeling study. The advection of negative η into the SH can be understood by examining the absolute vorticity equation. Again neglecting the frictional effects and horizontal gradients of vertical motion, the local rate of change of η is given by the sum of the advection of η by the total wind $(-\mathbf{V} \cdot \nabla\eta)$ plus the horizontal divergence term $(-\eta\nabla \cdot \mathbf{V})$. Our analysis indicates that in the lower troposphere (950 hPa) from equator to about 12°N, the meridional advection term $(-v\frac{\partial\eta}{\partial y})$ contributes negatively (areal mean value -1.1×10^{-10} s^{-2}). Therefore, from the absolute vorticity perspective, in the region from equator to 7°N, the meridional advection of η tends to decrease the local η. Note again that the meridional advection of η is the sum of advection of relative vorticity $(-v\frac{\partial\zeta}{\partial y})$ term and planetary vorticity $(\beta\, v)$ term. The net effect of the divergence term in the region from equator to 7°N (7°N to 12°N) tends to decrease (increase) the local η with areal mean value -0.6×10^{-10} s^{-2} (1.5×10^{-10} s^{-2}). It is therefore clear that both the meridional advection of η and the divergence term contribute in the advection of negative η from equator to about 7°N. From these DPV (MPV) distributions, it is therefore clear that (i) DSI (CSI) conditions are initiated preceding to the actual monsoon transition over the entire Asian monsoon region, and (ii) the negative advection of DPV (MPV) into the SH can be understood from the simplified absolute and potential vorticity budget equations.

3.2.3 Diabatic heating and meridional circulation

In the previous section, we noted that SI or CSI conditions become fully established preceding monsoon transition (11–15 May in the case of EAM and 21–25 May in the case of SAM). In Subsection 3.1, we have seen that the model monsoon transition takes place one or two pentads subsequent to the commencement of SI/CSI conditions. Having established that, we would like to unravel the connection between SI/CSI and diabatic heating. We will examine here the evolution of total diabatic heating and the vertical velocity distribution over the EAM and SAM regions before and after monsoon transition. The total diabatic heating is given by

$$\dot{Q}_{TH} = \dot{Q}_{LH} + \dot{Q}_{LWH} + \dot{Q}_{SWH} + \dot{Q}_{SH} \qquad (8)$$

where the subscripts *TH, LH, LWH, SWH* and *SH* respectively stand for total diabatic heating, latent heating, longwave heating, shortwave heating and sensible heating. Figure 6 shows the latitude-pressure cross section of the development of total diabatic heating (left panel) for all the pentads starting from 1–5 May to May 26–30 over the EAM region. The most conspicuous feature here is the abrupt increase of diabatic heating from $\approx$ 2–3 K day^{-1} preceding to transition (11–15 May) to $\approx$ 12 K day^{-1} at the time of transition (16–20 May). The diabatic heating is considerably weak in the first two pentads (see 1–5 May and 6–10 May) before the monsoon transition and by 11–15 May, a weak extended mid-tropospheric heat source begins to develop. By 16–20 May, an organized powerful mid-tropospheric asymmetric heat source (12 K day^{-1}) centered around 10°N is formed. The enhancement of diabatic heating from 11–15 May to 16–20 May is rather rapid and explosive. The heat source becomes more pronounced subsequent to the transition. By 26–30 May the primary heat source (16 K day^{-1}) (now centered around 5°N) splits to form a secondary one (14 K day^{-1}) (centered around 18°N).

The $y - p$ structure and evolution of vertical velocity (ω) over the EAM region is shown in Fig. 6 (right panel). One of the distinctive features here is the abrupt strengthening of the vertical motion (meridional circulation) in the pentad corresponding to monsoon transition (16–20 May). Vertical motions well before transition (1–5 May and 6–10 May) are very feeble with even downward motions over some regions 5° to 10° north of the equator (see 6–10 May). By 11–15 May, extended regions of large scale ascent slightly ahead of negative DPV and MPV (unstable SI and CSI) areas (see Fig. 4) have formed. At the monsoon transition (16–20 May), vertical motion is intensified by a factor of four from its preceding pentad (11–15 May). The vertical motions subsequent to transition (21–25 May and 26–30 May) are further reinforced (by a factor of five from 11–15 May values). The aforementioned results are evidence of the CISK-like positive feedback between diabatic heating distribution and vertical velocity distribution (monsoonal meridional circulation). The evolution of diabatic heating and vertical velocity distributions over the SAM region is similar to EAM except that the abrupt intensification of these fields takes place two pentads behind (not shown). Thus, it is sufficiently clear from the above discussion that (i) at the time of transition over the entire monsoon region, there is a rapid enhancement of diabatic heating as well as vertical motion, and (ii) preceding the monsoon transition diabatic heating and vertical motions over the monsoon region are significantly weaker. This raises an obvious question: what mechanism causes the explosive growth of diabatic heating at the time of transition? To investigate this issue further, we have presented the evolution of divergence distribution over the EAM and SAM regions for two contrasting states: (i) before, and (ii) after, monsoon transition.

A brief description of the scenario that causes the explosive growth of diabatic heating at the time of monsoon transition is provided here. The evolution of the divergence field over the EAM and SAM regions one to two pentads before the monsoon transition indicates broad regions of convergence. These regions extend from the equator to around 15°N from the lower troposphere to the mid-troposphere with maximum values distributed slightly ahead of the zero line of the DPV and MPV (unstable SI and CSI regions). In conjunction, an extended region of divergence exists from the equator to around 20°N between 400 hPa to 200 hPa (not shown). This extended lower (upper) tropospheric convergence (divergence) distribution can augment frictional convergence occurring near the boundary layer. The large scale moisture convergence forced as a consequence of the symmetrically unstable environment may strengthen further due to boundary layer frictional processes, which may result in condensation of moisture and further release of latent heat. The genesis of the weak heat source (11–15 May; see Fig. 6, left panel) seems to be the existence of negative DPV and MPV (unstable SI and CSI) regions in the SH. Since the lower tropospheric tropical atmosphere is largely conditionally unstable (Fig. 4, right panel), the existence of large scale low level convergence (resulting from SI and CSI) can favor CISK-like processes, eventually releasing large amounts of latent heat, thereby producing a strong heat source at the time of monsoon transition (16–20 May; see Fig. 6, left panel).

To gain further insight into the physical connection between symmetric instability and monsoon circulation at the time of transition, we illustrate here the interrelationship of the latitudinal position in the SH of (i) the zero DPV contour (which is a mea-

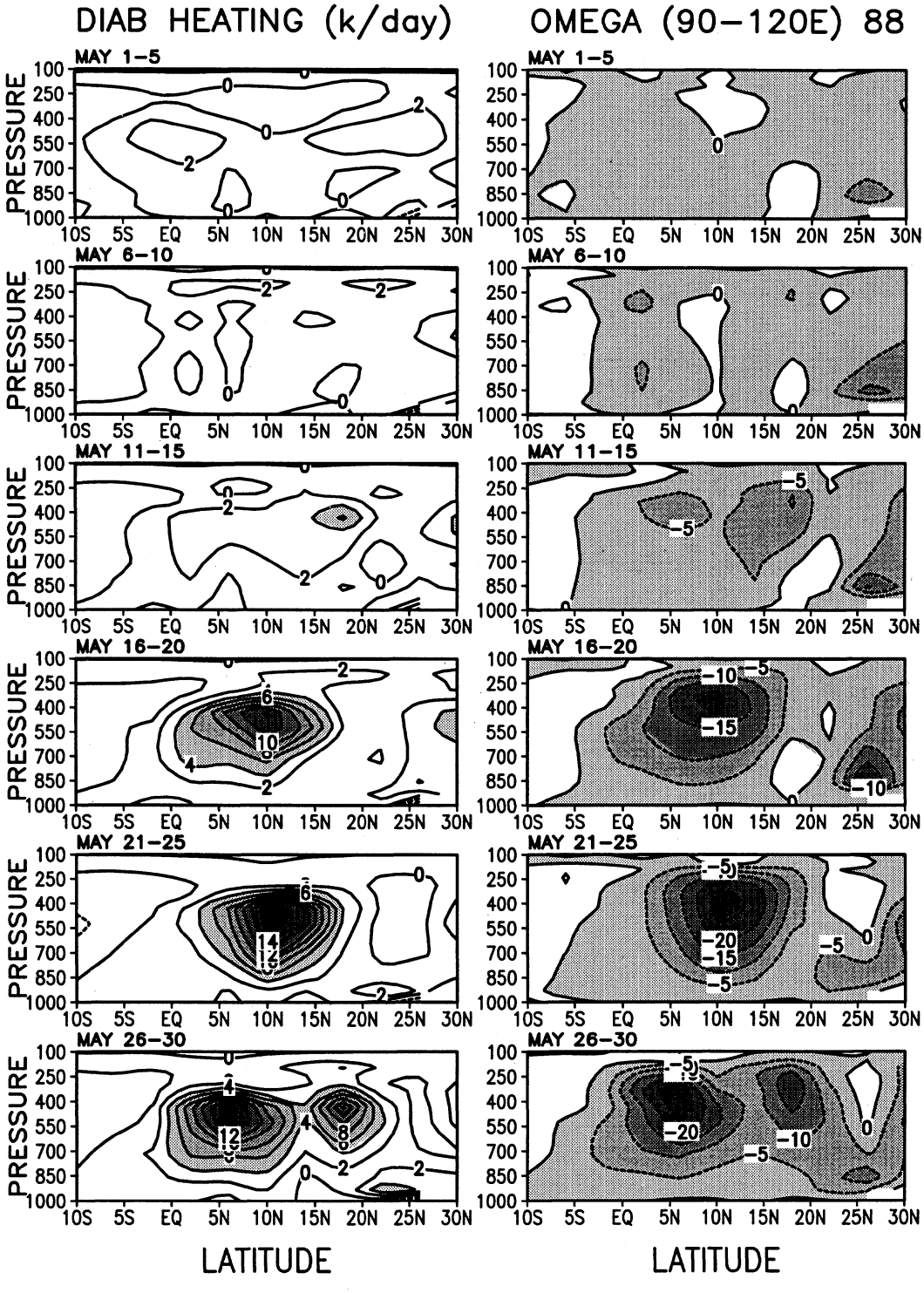

Fig. 6. Latitude-pressure cross sections of pentad mean total diabatic heating (left panels) and vertical velocity (right panels) fields over the EAM region for 1988. Contour intervals for the total diabatic heating and vertical velocity fields are respectively 2 K day^{-1} and -5×10^{-2} Pa s^{-1}. Values larger than 4 K day^{-1} are shaded (left panels) and shadings (right panels) denote a region of negative vertical velocity and values larger than -5×10^{-2} Pa s^{-1} are darkened.

sure of the latitudinal distribution of the area of SI) at 950 hPa, and (ii) the maximum convergence at 950 hPa *vs* maximum vertical motion of the monsoon circulation (which is a measure of the intensity of the meridional circulation) for all the pentads for the EAM. We also examine the relationship between maximum negative DPV in the SH (which is a measure of the strength of SI) and maximum vertical motion of the monsoon circulation. Figure 7a shows a scatter diagram between the latitudinal position of the zero DPV contour in the SH at 950 hPa (closed circle connected by a thick line) and maximum vertical velocity of the SH monsoon circulation plotted for all the pentads starting from 1–5 May till 26–30 May for the EAM region. It is clear that starting in 11–15 May (pentad 3), the zero DPV contour shifts up to 5°N into the SH and only weak vertical motions exist. The conditions change from the pre-transition state to the transition state (pentad 4) quite rapidly with negative DPV areas extending up to 7°N in conjunction with vertical motions increasing almost threefold. Maximum negative DPV advection, together with maximum vertical motions, occur after the transition (pentad 5). It is also of interest to note that the latitudinal position of the maximum convergence in the SH at 950 hPa (open triangle connected by a dotted line) generally leads the zero DPV contour position by about a degree, which implies that the low level convergence is a forced response of symmetric instability. The dynamical implication of the latitudinal position of the maximum vertical motion (maximum lower tropospheric convergence) is discussed in the framework of a multi-level linear model as well as in a simple dynamical balance condition in Subsubsection 3.3.2. Figure 7b shows the maximum vertical motion of the monsoon circulation plotted as a function of maximum negative DPV in the SH. Beginning in 11–15 May (pentad 3), the strength of instability reaches a value of -0.8×10^{-7} $m^2s^{-1}K\ kg^{-1}$, which is comparable to the value at the time of monsoon transition (-1.0×10^{-7} $m^2s^{-1}K\ kg^{-1}$). Subsequent to monsoon transition (pentad 5), the maximum DPV value reaches the peak (-2.5×10^{-7} $m^2s^{-1}K\ kg^{-1}$) together with a strong meridional circulation. Later on, the value decreases further.

In Figs. 8a–8b, we present respectively the latitude-pressure cross section of the divergence field before (1–5 May) and after (21–25 May) transition over the EAM region. The divergence field before the transition (Fig. 8a) shows that broad regions of weak convergence lie between 5°S to 15°N mainly in the lower troposphere, with a weak maximum slighly off the equator presumably forced by large scale premonsoonal flows. By 11–15 May, a convergence field (not shown) extends to the mid-troposphere and a pronounced increase of divergence is found aloft (see Fig. 2, right panel). This pattern seems to have

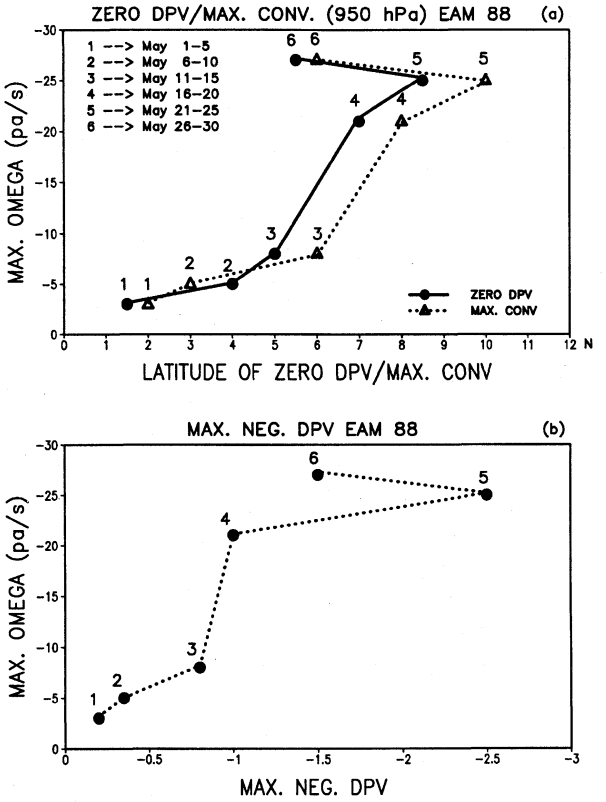

Fig. 7. (a) Scatter diagram between the latitudinal position in the SH of (i) the zero DPV contour at 950 hPa (thick solid line with closed circles, 10^{-7} K m^2 $kg^{-1}s^{-1}$) (ii) the maximum convergence at 950 hPa (dotted line with open triangles, 10^{-6} s^{-1}) and maximum vertical velocity (10^{-2} Pa s^{-1}) plotted for all the pentads starting from 1 (1–5 May) to 6 (26–30 May) over the EAM region for 1988 (b) maximum vertical velocity (10^{-2} Pa s^{-1}) plotted as a function of maximum negative DPV (10^{-7} Km^2 $kg^{-1}s^{-1}$) in the SH over the EAM region for 1988.

originated from unstable SI and CSI regions as depicted in the DPV and MPV distribution (see Fig. 4). The divergence field after the transition (Fig. 8b) shows that the off-equatorial convergence field located between 5°N and 17°N and 1000 hPa and 500 hPa, intensifies substantially with a maximum located around 10°N and 900 hPa. The pronounced upper tropospheric divergence field and the associated outflow is located directly above the lower tropospheric convergence field. It is important to note that the lower tropospheric organized convergence lies ahead of the unstable SI and CSI regions.

Figures 8c–8d show respectively the y-p cross section of the divergence field before (6–10 May) and after (6–10 June) transition over the SAM region. Extended low level weak convergence and moderate upper level divergence patterns are seen before tran-

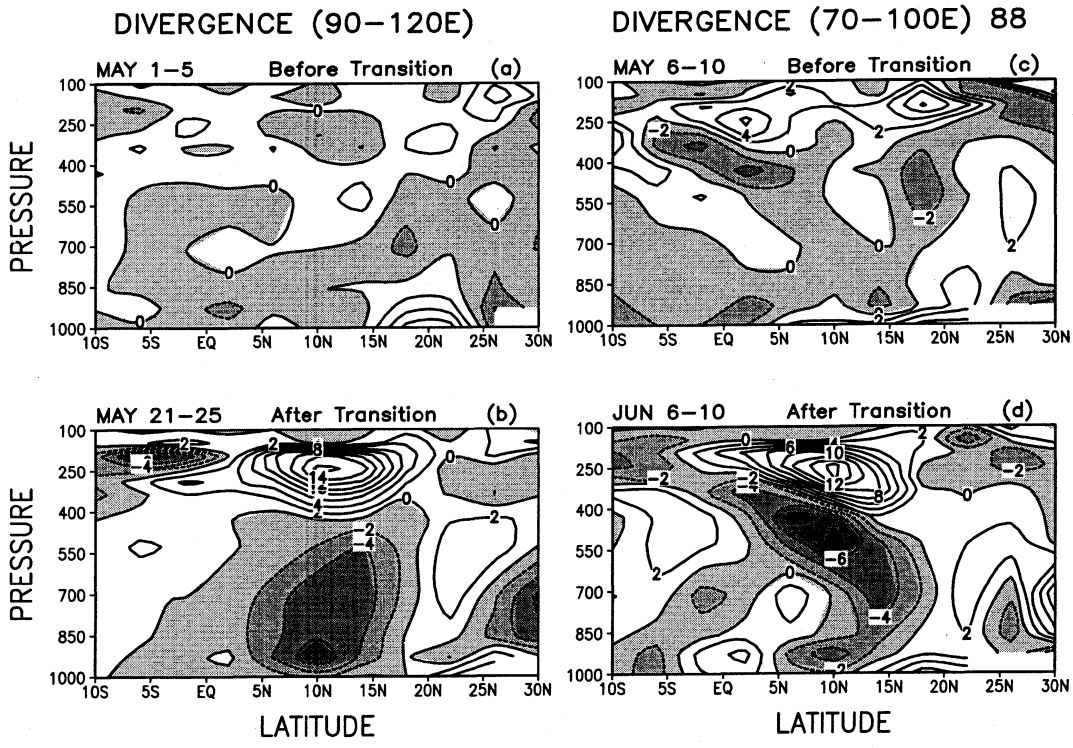

Fig. 8. Latitude-pressure cross sections of pentad mean divergence field (i) (a) before and (b) after transition over the EAM region (ii) (c) before and (d) after transition over the SAM region for 1988. Contour interval for the divergence field is 2×10^{-6} s^{-1}. Shadings denote a region of convergence and values larger than -2×10^{-6} s^{-1} are darkened.

sition (Fig. 8c). Convergence maximum is located in the upper troposphere, between 5°S to 5°N. The convergence and divergence distribution is stronger than the corresponding distribution for the EAM region (Fig. 8a). The center of the lower (upper) tropospheric convergence (divergence) maximum shifts by about 7° to 10° into the SH precede the monsoon transition (21–25 May), in conjunction with the negative DPV (MPV) advection nearly perpetually leading the zero line of the DPV (MPV) (not shown). The convergence and divergence pattern become more intensified after the transition with strong lower and mid-tropospheric convergence and vigorous upper tropospheric divergence values with maxima located ahead of the zero line of the DPV (MPV) pattern (Fig. 8d).

3.3 The response of monsoon circulation to asymmetric diabatic forcing

3.3.1 Nonlinear relationship between diabatic heating and meridional circulation

In the presence of interactive heating and viscous effects, one of the main issues is to examine the existence of any threshold behavior marking the onset of monsoonal meridional circulation. We will first examine the results from the GLA GCM over the EAM and SAM regions. Figures 9a–9b show respectively the maximum diabatic heating rate (K day^{-1}) and maximum vertical motion (Pa s^{-1}) plotted as a function of time in pentads starting from 1–5 May to 16–20 June for the EAM (thick dotted line) and SAM (thick solid line) regions. Over the EAM region, a sharp increase in magnitude of diabatic heating occurs at the pentad 4 (16–20 May) with a value of 12 K day^{-1} from the previous pentad (11–15 May) with a value of 5 K day^{-1} (see Fig. 9a, dotted line). The associated vertical motions essentially show similar behavior, *i.e.*, an abrupt enhancement of vertical motions at pentad 4 with a value of -21×10^{-2} Pa s^{-1} from the previous pentad (11–15 May) with a value of -8×10^{-2} Pa s^{-1}(see Fig. 9b, dotted line). The diabatic heating rate reaches a peak at pentad 5 (21–25 May) and plateaus till pentad 7 (1–5 June). Almost similar behavior can be seen with the vertical motions. A fully developed meridional circulation originates only at pentad 4 when the diabatic forcing magnitude exceeds some threshold value of around 5 K day^{-1} (see Figs. 2 and 6, right panels).

Over the SAM region, diabatic heating magnitudes and the associated vertical motions have generally higher values compared to the EAM region from pentads 1 to 3, which indicates that an organized meridional circulation of moderate intensity originates much prior to the actual date of monsoon transition, which is at pentad 7 (1–5 June). An

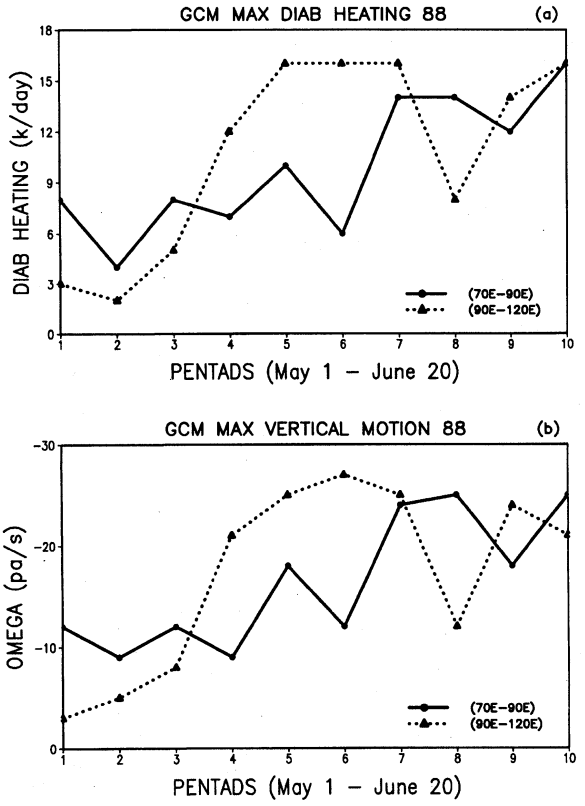

Fig. 9. Maximum value of the (a) total diabatic heating rate (K day^{-1}) and (b) vertical motion (10^{-2} Pa s^{-1}) from the GLA GCM for 1988, plotted as a function of time in pentads starting from 1–5 May to 16–20 June. Thick dotted line with closed triangles is for the EAM region and thick solid line with closed circles is for the SAM region.

abrupt increase in diabatic heating occurs at pentad 7 (1–5 June) with a value of 14 K day^{-1} from the previous pentad (26–30 May) with a value of 6 K day^{-1}. Diabatic heating and the associated vertical motions have a large fluctuation from pentads 1 to 6 over the SAM region. This fluctuation arises due to the effect of gravity wave drag in the GLA GCM. This is confirmed by a separate numerical investigation without incorporating gravity wave drag, which is reported in another study.

The evolution of diabatic heating distribution reveals that a threshold in the off-equatorial diabatic heating exists with some critical value less than 5 K day^{-1} (see Fig. 6) at the time of monsoon transition. The model transition is quite pronounced over the EAM region (see thick dotted line between pentads 3 and 4 in Figs. 9a–9b). The diabatic heating magnitudes and the associated vertical motions over the SAM have considerably higher values compared to the threshold values over EAM that will establish a meridional circulation with moderate strength prior to the actual monsoon transition. Therefore, the transition here is less pronounced (see thick solid line between pentads 6 and 7 in Figs. 9a–9b). It should be noted that the magnitude of the critical thermal forcing is dependent on viscosity and also on the width of the heating region and therefore a direct comparison of the nonlinear evolution of GLA GCM results with PH92 would be difficult. The simulated heat source at the time of transition is centered around 10°N with a half-width of around 15° as shown in Fig. 6 (see 16–20 May; left panel). The evolution of diabatic heating and vertical motion fields show a nonlinear relationship with a threshold behavior somewhat similar to PH92. It may be recalled that PH92 assumes an external heat source positioned off the equator and, therefore, cannot explain the origin and location of the off-equatorial thermal forcing. As noted in Subsection 3.2, the origin of off-equatorial strong thermal forcing at the time of transition is primarily due to the onset of SI (CSI) conditions preceding the monsoon transition.

3.3.2 Linear model results

A linear, multi-level, steady-state zonally symmetric model similar to KL (see Appendix for details) is used to examine distinctly the steady state dynamical response of the symmetric atmosphere to an idealized asymmetric thermal forcing in the presence of monsoonal basic states. In the idealized study, we have considered responses of a zonally symmetric atmosphere by varying both the location and magnitude of an idealized asymmetric thermal forcing. The idealized thermal forcing is specified by the following expression

$$Q(y,p) = \begin{cases} Q_\circ \cos^2\left(\dfrac{\pi}{2}\dfrac{\varphi-\varphi_c}{\nabla\varphi}\right)\sin\left(\dfrac{\pi p}{p_\circ}\right), \\ \varphi_c - \nabla\varphi \le \varphi \le \varphi_c + \nabla\varphi \\ 0, \text{ otherwise} \end{cases} \tag{9}$$

where $Q_\circ$ is the amplitude of the thermal forcing, which is varied from 2 K day^{-1} to 20 K day^{-1}, φ_c is the latitude where the forcing is centered, which is varied from equator to 30°N in increments of 2°, and $\nabla\varphi$ is the heating width which is chosen to be 16° in this analysis. The vertical heating distribution ($\sin(\pi p/p_\circ)$ term in (9)) has a maximum at 500 hPa, which is typical of the observed monsoonal diabatic heating (Schaack *et al.*, 1990). The horizontal heating distribution ($\cos^2$ term in (9)) is used for generating an off-equatorial heating symmetric with respect to φ_c. Thus, by varying φ_c and $Q_\circ$, we are able to consider idealized off-equatorial heating (mimicking the asymmetric monsoonal heating; see Fig. 6, left panel) centered at different latitudes with different strengths. Next, we will present the linear, steady-state response results of the multi-level zonally symmetric model by varying φ_c and $Q_\circ$ in the presence of monsoonal zonal flow of 16–20 May, 1988. Figure 10a shows the maximum vertical mo-

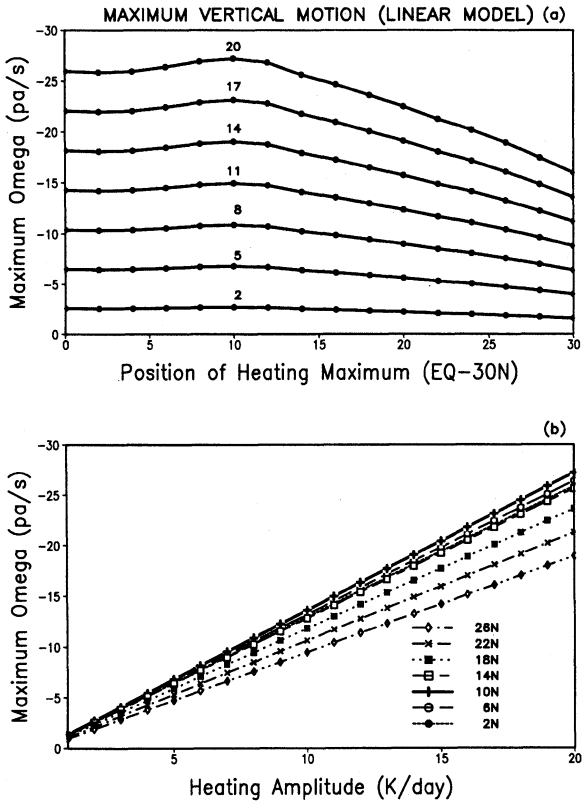

Fig. 10. Maximum vertical velocity ($\omega_{\max}$)(10^{-2} Pa s^{-1}) obtained as the response from the linear model plotted as a function of (a) the latitudinal position (from equator to 30°N) of heating maximum for a range of heating amplitude values starting from 2 K day^{-1} to 20 K day^{-1} in increments of 3 K day^{-1}. (b) the heating amplitude (K day^{-1}) for a range of latitudinal positions of heating maximum starting from 2°N to 26°N in increments of 4°N.

tion of the meridional circulation ($\omega_{\max}$) plotted as a function of the meridional position of the heating maximum (φ_c) for a range of thermal forcing amplitudes (Q_o). Figure 10b shows $\omega_{\max}$ plotted as a function of Q_o for different values of φ_c. It is interesting to note from Figs. 10a–10b that $\omega_{\max}$ values distinctly peak around 10°N for a range of Q_o values starting from 5 K day^{-1} to 20 K day^{-1}. Examination of Figs. 10a–10b suggests that maximum efficiency of vertical motion is achieved when the thermal forcing is positioned around 10°N. Shifting the location of the heating maximum to around 10°N results in about 45 % increase in the maximum vertical motion when compared to the case when the heating maximum is located poleward of 25°N. The most notable feature emerging from these thermally forced idealized experiments is a narrow preferential latitudinal zone (5° to 6° meridional width) located at about 10°N where the thermodynamical response, originating from the heat source positioned at about 10°N, is at its maximum efficiency in producing the most intense meridional circulation. For an off-equatorial asymmetric thermal forcing, in the absence of boundary layer frictional effects, the steady state zonally symmetric dynamical model response may result from a subtle balance between

$$\beta v = -f\left(\frac{\partial v}{\partial y}\right) \tag{10}$$

where (βv) is the advection of planetary vorticity and ($-f\partial v/\partial y$) is the divergence term. Over the tropics, the horizontal thermal advection is generally small as the temperature gradient is small and therefore the general balance in the thermodynamic energy equation is between

$$-\left(\frac{\sigma p}{R}\right)\omega \simeq \left(\frac{\dot{Q}}{C_p}\right) \tag{11}$$

where the term on the left is the adiabatic cooling associated with the ascending motion and the term on the right is the diabatic heating. Since the vertical p-velocity ω is the vertical integral of horizontal divergence, $\omega_{\max}$ therefore would depend on the subtle balance relation (10). It is clear from the linear model response results that the most intense meridional circulation is generated when the off-equatorial thermal forcing location lies centered around 10°N. It should be noted that the genesis and further growth of the off-equatorial heating positioned at about 10°N at the time of monsoon transition is attributed to SI (CSI) conditions in the near equatorial SH. It is also interesting to note from the linear model perspective that maximum efficiency of vertical motion is accomplished when the off-equatorial heat source is positioned at about 10°N.

4. Discussion and conclusions

In this study, we have investigated the physical connections between SI/CSI and onset of the Asian monsoon, using the GLA GCM, with a view (i) to elucidate the causal relationship between SI/CSI and monsoon onset, and (ii) to investigate the threshold behavior of the off-equatorial thermal forcing in the overall perspective of SI/CSI. The key findings of this study can be summarized as follows:

Results from two numerical simulations for the years 1987 and 1988 exhibit an abrupt increase in rainfall at the time of model monsoon onset, which happens around (i) mid of May (16–20 May) for the EAM and (ii) beginning of June (1–5 June) for the SAM regions. Monsoon transition, as depicted by the rapid northward progression of the axis of the maximum vertical motion and the associated cloud bands (ITCZ) from one latitudinal position to another, occurs during 16–20 May for the EAM and

1–5 June for the SAM regions for the year 1988. Barotropic and baroclinic shears originate 5 to 10 days preceding the actual monsoon transition, which then becomes very pronounced at the time of transition and continues with the same or enhanced intensities for the later periods.

Examination of the necessary stability criterion for dry SI (CSI) over the EAM region reveals a sudden cross equatorial advection of negative DPV (MPV) into the SH, 5 to 10 days preceding the model monsoon transition, thereby setting the condition for dry (moist) SI. During the model monsoon transition, meridional and vertical extensions of symmetrically unstable regions transpire. Maximum shift of the zero line of DPV and MPV (dry and moist symmetrically unstable regions) develops subsequent to monsoon transition. The model tropical (monsoonal) lower tropospheric atmosphere is found to be largely conditionally unstable (CI). The negative MPV regions devoid of CI are characteristic of CSI where slantwise overturning occurs. We have differentiated such unstable CSI regions. Similar intriguing features are found over the SAM regions, except that the negative DPV/MPV advection initiates three/four pentads prior to SAM transition. Detailed analysis of the PV budget equation indicates that the advection of negative lower tropospheric PV into the SH is mostly controlled by the dominance of vertical differential diabatic heating over horizontal differential diabatic heating. The key feature that emerges from the analyses of SI (CSI) stability criterion over the EAM and SAM regions is that SI (CSI) commences preceding the actual monsoon transition.

In order to investigate the physical connection between SI/CSI and asymmetric thermal forcing, we have analysed the evolution of total diabatic heating and vertical velocity distribution (meridional circulation) over the EAM and SAM regions. One of the most intriguing features over the EAM is the abrupt and rather explosive enhancement of diabatic heating from 2–3 K day^{-1} prior to transition to 12–14 K day^{-1} at the time of transition. A similar distinctive feature in the vertical motion field is the abrupt strengthening of the meridional circulation at the time of monsoon transition. The centers of maximum vertical motions are located slightly ahead of negative DPV and MPV (unstable SI and CSI regions) areas in the SH. The divergence field before and after monsoon transition reveals that maximum convergence (divergence) in the lower (upper) troposphere is located slightly poleward of the zero line of DPV and MPV as a forced response to symmetric instability conditions. The genesis of the pre-monsoon weak heat source seems to be originating because of the existence of negative DPV and MPV regions in the near equatorial SH. The lower tropospheric conditionally unstable tropical atmosphere, in the presence of off-equatorial large scale lower (upper) tropospheric convergence (divergence), is conducive to excite CISK-like processes that may eventually release large amounts of latent heat and develop strong heat source at the time of monsoon tranistion. The explosive growth from a state of weak heat source (preceding to monsoon transition) to a strong heat source (during monsoon transition) is a manifestation of SI and CSI in the near equatorial SH. Similar characteristics are found over the SAM region, except that the abrupt intensification of diabatic heating and vertical motion happens two pentads behind. The interrelationship between the location of zero DPV/MPV contour and lower tropospheric maximum convergence versus maximum vertical motion of the monsoonal circulation in the SH clearly illustrates the physical connection between SI and monsoon onset, showing that SI is a causal mechanism for the onset of monsoon.

The response of monsoon circulation to asymmetric diabatic forcing in the GLA GCM reveals that a fully developed meridional circulation at the time of monsoon transition originates only when the diabatic forcing magnitude exceeds some threshold value of around 5 K day^{-1}. This model transition is quite pronounced over the EAM region, whereas over the SAM region the transition is less pronounced. The genesis and further growth of the off-equatorial thermal forcing arise primarily due to the presence of dry (moist) symmetrically unstable regions in the near equatorial SH.

In the framework of a steady state multi-level linear model, by varying both the location and magnitude of an idealized asymmetric thermal forcing (mimicking the asymmetric monsoonal heating), we have studied the dynamical responses of a zonally symmetric atmosphere in the presence of basic flows. The most distinctive feature of the linear model response is a limited preferential latitudinal zone around 10°N where the thermodynamical response, resulting from the heat source positioned at about 10°N, is at its maximum efficiency in producing the most intense meridional circulation. Shifting the location of the heating maximum to around 10°N results in about a 45 % increase in the maximum vertical motion than the case when the heating maximum is positioned poleward of 25°N. The steady state zonally symmetric model response may be due to a subtle balance between advection of planetary vorticity and horizontal divergence terms.

Our detailed theoretical and modeling studies, using a simple linear and a comprehensive GCM, demonstrate that SI (CSI) of zonal monsoon flows is a causal mechanism in explaining the monsoon transition. More detailed observational, theoretical, diagnostic and high-resolution modeling studies should be performed to fully understand the various intricacies involved in this intriguing phenomena.

Acknowledgments

The insightful comments of the two anonymous reviewers on the earlier version of the manuscript are gratefully acknowledged. We are grateful to Dr. K. Saito, Editor, JMSJ for his helpful comments. We thank Drs. Y.C. Sud, L. Peng, W.C. Chao and S. Yang for many fruitful discussions. This work is supported in part by the NASA Atmospheric Modeling and Data Analysis Program and the Earth Observing System Interdisciplinary Investigation.

Appendix

The zonally symmetric primitive equation model is essentially equivalent to that used by KL. Following KL's linearized system of equations (Eq. (1)–(4)) except with the omission of interactive cumulus heating formalism, the final equation obtained is

$$\left\{-\frac{\partial^2}{\partial t^2} - f\left(f - \frac{\partial U}{\partial y}\right)\right\}\frac{\partial^2\psi'}{\partial p^2} - \beta\frac{\partial U}{\partial p}\frac{\partial\psi'}{\partial p} - 2f\frac{\partial U}{\partial p}\frac{\partial}{\partial p}\left(\frac{\partial\psi'}{\partial y}\right) - f\frac{\partial^2 U}{\partial p^2}\frac{\partial\psi'}{\partial y} - \sigma\frac{\partial^2\psi'}{\partial y^2} = \frac{R}{pC_p}\frac{\partial\dot{Q}'}{\partial y} \quad (1)$$

Equation (1) is the counterpart of Eq. (9) of KL. The steady state equation is obtained by zeroing the time derivatives. Data for $\dot{Q}'(y,p)$, $U(y,p)$ and $\sigma(p)$ are taken either from the nonlinear model simulation or from idealized distributions as mentioned earlier. Employing central differencing for meridional and vertical derivatives with appropriate boundary conditions, the system of equations (1) at all latitude×pressure grid points can be put into the form

$$(\widetilde{A})\widehat{Z} = \widehat{B} \quad (2)$$

where $\widetilde{A}$ is a real square matrix, $\widehat{Z}$ and $\widehat{B}$ are the column vectors. The column vectors $\widehat{Z}$ and $\widehat{B}$ are respectively the unknown eigenfunction and the known diabatic heating function. Equation (2) is a well-known problem which can be efficiently solved by the standard numerical methods.

References

Ananthakrishnan, R., V. Srinivasan, A.R. Ramakrishnan and R. Jambunathan, 1968: Synoptic features associated with the onset of southwest monsoon over Kerala. *India Meteorological Department Forecasting Manual*, **No. IV-18.2**.

Bennetts, D.A. and B.J. Hoskins, 1979: Conditional symmetrical instability-a possible explanation for frontal rainbands. *Quart. J. Roy. Meteor. Soc.*, **105**, 945–962.

Charney, J.G., 1973: Planetary fluid dynamics. *Dynamic Meteorology*: Lecture Delivered at the Summer School of Space Physics of the Centre National d'etudes Spatiales, Lammion, France, P. Morel, Ed., D. Reidel, 622 pp.

Dunkerton, T.J., 1981: On the inertial stability of the equatorial middle atmosphere. *J. Atmos. Sci.*, **38**, 2354–2364.

Dunkerton, T.J., 1993: Inertial instability of nonparallel flow on an equatorial β plane. *J. Atmos. Sci.*, **50**, 2744–2758.

Eliassen, A., 1952: Slow thermally or frictionally controlled meridional circulation in a circular vortex. *Astrophy. Norv.*, **5**, 60 pp.

Emanuel, K.A., 1979: Inertial instability and mesoscale convective systems. Part I: Linear theory of inertial instability in rotating viscous fluids. *J. Atmos. Sci.*, **36**, 2425–2449.

Emanuel, K.A., 1983: The Lagrangian parcel dynamics of moist symmetric instability. *J. Atmos. Sci.*, **40**, 2368–2376.

Fennessy, M.J., J.L. Kinter, B. Kirtman, L. Marx, S. Nigam, E.K. Schneider, J. Shukla, A. Vernekar, Y. Xue and J. Zhou, 1994: The simulated Indian monsoon: A GCM sensitivity study. *J. Climate.*, **7**, 33–43.

Held, I.M. and A.Y. Hou, 1980: Nonlinear axially symmetric circulations in a nearly inviscid atmosphere. *J. Atmos. Sci.*, **37**, 515–533.

Hirasawa, N., K. Kato and T. Takeda, 1995: Abrupt change in the characteristics of the cloud zone in subtropical east Asia around the middle of may. *J. Meteor. Soc. Japan*, **73**, 221–239.

Holton, J.R., 1992: *An introduction to dynamic meteorology*, Academic Press, 3rd ed, 511pp.

Hoskins, B.J., 1974: The role of potential vorticity in symmetric stability and instability. *Quart. J. Roy. Meteor. Soc.*, **100**, 480–482.

Hou, A.Y. and R.S. Lindzen, 1992: The influence of concentrated heating on the Hadley circulation. *J. Atmos. Sci.*, **49**, 1233–1241.

Kim, J.H. and Y.C. Sud, 1993: Circulation and rainfall climatology of a 10-year (1979–1988) integration with the Goddard Laboratory for Atmospheres General Circulation Model. *NASA Tech. Memo.*, **No. 104591**, NASA Goddard Space Flight Center, Greenbelt, Maryland.

Krishnakumar, V. and R.N. Keshavamurty, 1993: Symmetric instability of monsoon zonal flows. *Atmósfera*, **6**, 135–144.

Krishnakumar, V. and K.M. Lau, 1997: Symmetric instability of monsoon flows. *Tellus*, **49**, 228–245.

Krishnamurti, T.N., H.S. Bedi and M. Subramaniam, 1989: The summer monsoon of 1987. *J. Climate.*, **2**, 321–340.

Krishnamurti, T.N., H.S. Bedi and M. Subramaniam, 1990: The summer monsoon of 1988. *Meteorol. Atmos. Phys.*, **42**, 19–37.

Kuo, H.-L., 1954: Symmetric disturbances in a thin layer of fluid subject to a horizontal temperature gradient and rotation. *J. Meteor.*, **11**, 399–411.

Lau, K.M., 1992: East Asian summer monsoon rainfall variability and climate teleconnection. *J. Meteor. Soc. Japan*, **70**, 211–242.

Lau, K.M. and S. Yang, 1996: Seasonal variation, abrupt transition and intraseasonal variability associated

with the Asian summer monsoon in the GLA GCM. *J. Climate.*, **9**, 965–985.

Lau, K.M. and M.T. Li, 1984: The monsoon of east Asia and its global association — a survey. *Bull. Amer. Meteor. Soc.*, **65**, 114–125.

Lau, K.M., G. Yang and S.H. Shen, 1988: Seasonal and intraseasonal climatology of summer monsoon rainfall over East Asia. *Mon. Wea. Rev.*, **116**, 18–37.

Lindzen, R.S. and A.Y. Hou, 1988: Hadley circulations for zonally averaged heating centered off the equator. *J. Atmos. Sci.*, **45**, 2416–2427.

Ooyama, K., 1966: On the stability of the baroclinic circular vortex: A sufficient condition for instability. *J. Atmos. Sci.*, **23**, 43–53.

Palmer, T.N., C. Brankovic, P. Viterbo and M.J. Miller, 1992: Modeling interannual variations of summer monsoons. *J. Climate.*, **5**, 399–417.

Persson, P.G. and T.T. Warner, 1995: The nonlinear evolution of idealized, unforced, conditional symmetric instability: A numerical study. *J. Atmos. Sci.*, **52**, 3449–3474.

Plumb, R.A. and A.Y. Hou, 1992: The response of a zonally symmetric atmosphere to subtropical thermal forcing: Threshold Behavior. *J. Atmos. Sci.*, **49**, 1790–1799.

Satoh, M., 1994: Hadley circulations in radiative-convective equilibrium in an axisymmetric atmosphere. *J. Atmos. Sci.*, **51**, 1947–1968.

Sawyer, J.S., 1949: The significance of dynamic instability in atmospheric motions. *Quart. J. Roy. Meteor. Soc.*, **75**, 364–374.

Schaack, T.K., D.R. Johnson and M.Y. Wei, 1990: The three-dimensional distribution of atmospheric heating during the GWE. *Tellus*, **42**, 305–327.

Schneider, E.K. and R.S. Lindzen, 1977: Axially symmetric steady state models of the basic state of instability and climate studies. Part I: Linear calculations. *J. Atmos. Sci.*, **34**, 253–279.

Solberg, M., 1936: Le mouvement d'inertie de l'atmosphere stable et son role dans le theorie des cyclones. *Union Geodesique et Geophisique internationale VIeme assemblee, Edinburg, Vol. II*, 66–82.

Stevens, D.E., 1983: On symmetric stability and instability of zonal mean flow near the equator. *J. Atmos. Sci.*, **40**, 882–893.

Stone, P.H., 1966: On non-geostrophic baroclinic stability. *J. Atmos. Sci.*, **23**, 390–400.

Sud, Y.C., W.C. Chao and G.K. Walker, 1991: Contributions to the implementation of Arakawa-Schubert cumulus parameterization in the GLA GCM. *J. Atmos. Sci.*, **48**, 1573–1586.

Sud, Y.C. and G.K. Walker, 1993: A rain evaporation and downdraft parameterization to complement a cumulus updraft scheme and its evaluation using GATE data, Mon. Wea. Rev., **121**, 3019–3039.

Sun, W.Y., 1984: Rainbands and symmetric instability. *J. Atmos. Sci.*, **41**, 3412–3426.

Tomas, R.A. and P.J. Webster, 1997: The role of inertial instability in determining the location and strength of near-equatorial convection. *Quart. J. Roy. Meteor. Soc.*, **123**, 1445–1482.

Xu, Q., 1986: Conditional symmetric instability and mesoscale rainbands. *Quart. J. Roy. Meteor. Soc.*, **112**, 315–334.

Yang, S., K.M. Lau and M. Sankar-Rao, 1996: Interannual variability of the Asian summer monsoon: Precursory signals associated with the interannual variability of the Asian summer monsoon. *J. Climate.*, **9**, 949–964.

Young, J.A., 1981: Low-level summer monsoon circulations. *Proceedings of the international conference on early results of FGGE and large-scale aspects of its monsoon experiments, Tallahassee*, **5.4-5.11**, Geneva, Switzerland.

Waliser, D.E. and R.C.J. Somerville, 1994: Preferred latitudes of the intertropical convergence zone. *J. Atmos. Sci.*, **51**, 1619–1639.

Zhou, J., Y.C. Sud and K.M. Lau, 1996: Impact of orographically induced gravity wave drag in the GLA GCM. *Quart. J. Roy. Meteor. Soc.*, **122**, 903–927.

アジアモンスーンのオンセットと突然遷移における対称不安定の役割の可能性

Vattompadam Krishnakumar・Ka-Ming Lau

(NASA ゴダード宇宙飛行センター)

乾燥/湿潤 (条件付き) 対称不安定 (SI/CSI)、赤道外非断熱熱強制とアジアモンスーンオンセットの物理的関係を、ゴダード大気研究室大循環モデル (GLA GCM) を用いて調べた。研究の目的は、SI/CSI とモンスーンオンセットの因果関係を解明することと、SI/CSI の条件下での非対称モンスーン熱強制の臨界的な振る舞いを調査すること、の 2 つである。これらは北方夏季モンスーン基本場での SI/CSI が、モンスーン突然遷移のもっともらしい説明かも知れないという著者のこれまでの線形不安定解析の結果を補強するものである。

鉛直運動最大軸の赤道から高緯度への急激な子午面移動で示されるモデルでのモンスーン遷移は、東アジアモンスーン (EAM) 域では 5 月 16 ～ 20 日、南アジアモンスーン (SAM) 域では 6 月 1 ～ 5 日に生じる。EAM と SAM 域上での乾燥 (湿潤)SI に要する安定基準は、モデルでのモンスーン遷移に 5 ～ 10 日先

立つ負の乾燥ポテンシャル渦度 (DPV) と湿潤ポテンシャル渦度 (MPV) の赤道を横切る夏半球への突然移流と、それによる SI/CSI 条件のセッティングを示している。DPV と MPV の零線 (乾燥/湿潤対称不安定域) の最大の移動はモンスーン遷移に続いて発生する。ポテンシャル渦度収支の簡単な解析によれば、夏半球への下部対流圏の負の PV 移流は鉛直方向の非断熱加熱の差が水平方向よりも大きいことによっている。

モンスーン遷移前後では非断熱加熱も 1 ~ 3 K/day から 12 ~ 14 K/day へ急変する。プレモンスーン期の弱い熱源の始まりは主に基本場の SI と CSI に起因し、ある程度大きなスケールの下部 (上部) 対流圏収束 (発散) パターンを作る。下部対流圏の条件付き不安定な熱帯大気は、赤道外の大規模下部 (上部) 対流圏収束 (発散) が存在すると、モンスーン遷移期に多くの潜熱を解放して強い熱源を発達させる CISK 状の過程を励起するのに役立っている。モデルの子午面循環は、非断熱強制がモンスーン遷移期に 5 K/day のしきい値を超えるときに始まる。モデルの遷移は EAM 域で SAM 域よりも明白である。理想化した非対称熱強制の位置と大きさの変化に対する帯状対称大気の線形定常状態での力学レスポンスは、最も強い子午面循環 (鉛直運動の最大効率) は熱強制が 10 N 付近にあるときに生じることを示す。DPV/MPV のゼロ線の位置、下部対流圏の最大収束と夏半球におけるモンスーン循環の最大鉛直風の関係は、帯状モンスーン流の SI(CSI) がモンスーン遷移オンセットの原因であることを明白に示唆している。